Sensors and Materials, Vol. 38, No. 4 (2026) 2069–2083
MYU Tokyo

S & M 4423

Enhancement of Vulnerability-informed Energy Storage System Using Improved Rapidly Exploring Random Tree Optimizer

Lingling Li,[1,2] Weiming Chen,[1,2] Hsiung-Cheng Lin,[3*] and Guangyuan Tian[4]

[1]State Key Laboratory of Intelligent Power Distribution Equipment and System, Hebei University of Technology, Tianjin 300401, China
[2]Key Laboratory of Electromagnetic Field and Electrical Apparatus Reliability of Hebei Province, Hebei University of Technology, Tianjin 300401, China
[3]Department of Electronic Engineering, National Chin-Yi University of Technology, Taichung 41170, Taiwan
[4]State Grid Chengde Power Supply Company, Chengde, Hebei 067060, China

(Received December 20, 2025; accepted February 27, 2026)

Keywords: distribution network, energy storage planning, system vulnerability, sensor, IRRTO

As renewable energy sources have been widely integrated into power distribution systems, alleviating power system vulnerability and reducing voltage deviation while lowering costs still remain important issues to be resolved in a power grid. For this reason, a vulnerability-aware energy storage planning framework is proposed for enhancing renewable-rich distribution networks. First, a vulnerability indicator system is established by considering both line and node operational states for vulnerability assessments. Second, an optimization model is formulated to minimize system vulnerability and life-cycle economic cost by incorporating objective functions and system operating constraints. Third, to efficiently implement the proposed model, an improved rapidly exploring random tree optimizer (IRRTO) is introduced on the basis of cubic chaotic mapping, a step-size learning factor, and a Lévy flight perturbation mechanism. Empirical validation is presented via simulations on the IEEE 33-bus system equipped with photovoltaic and wind power sources, confirming the effectiveness of the proposed methodology. Performance results verify that, compared with the case with no energy storage, the proposed model can reduce the power system vulnerability and voltage deviation up to 23.0 and 27.0%, respectively, while requiring lower investment and operating costs.

1. Introduction

As the global shift toward low-carbon and sustainable energy systems advances, distributed renewable generation is being adopted at an increasing rate in distribution networks.[1,2] However, the intermittency and volatility of renewable generation aggravate the vulnerability in distribution networks. Accordingly, energy storage systems (ESSs) are widely used as an effective strategy to enhance the power regulation capability.[3,4] In general, the state of charge and power states of distributed ESSs are monitored by embedded sensors, enabling the real-time tracking of power storage system charging–discharging processes.

*Corresponding author: e-mail: hclin@ncut.edu.tw
https://doi.org/10.18494/SAM6139

ISSN 0914-4935

In recent years, vulnerability-aware planning and operation of distribution networks have attracted increasing attention.[5,6] For example, Huang *et al.* proposed a vulnerability-aware dynamic reconfiguration framework incorporating hybrid energy storage sizing to mitigate wind power fluctuations and enhance system resilience.[7] Wang *et al.* developed a distribution network vulnerability index based on Theil's entropy of voltage and a modified Gini coefficient to quantify nodal power supply reliability and support restoration-oriented energy storage modeling.[8] Ullah *et al.* integrated vulnerability analysis into renewable generation and energy storage siting by evaluating voltage collapse proximity and fault probabilities, thereby improving network stability under extreme conditions.[9] Nevertheless, most existing approaches were focused on either nodal vulnerability or specific operating scenarios. Therefore, a unified framework to simultaneously coordinate line and node vulnerabilities on the basis of energy storage planning remains insufficient.

From an algorithmic perspective, a variety of metaheuristic methods were applied to address energy storage planning and operational challenges in contemporary distribution grids.[10,11] Ji *et al.* employed a multi-objective Coati Optimization Algorithm for optimizing photovoltaic energy storage operations.[12] Ali *et al.* proposed an improved large-scale multi-objective evolutionary algorithm to address distributed energy resource planning and battery management problems.[13] Belbachir *et al.* introduced a long-term memory artificial hummingbird algorithm to optimize the energy management of hybrid wind–battery systems under load and source uncertainties.[14] Although these methods presented promising performance in certain functions, challenges remain in balancing global exploration and local exploitation. In other words, it still lacks efficient handling of coupled objectives in vulnerability and economic issues.

This paper has the following structure. In Sect. 2, we introduce the vulnerability assessment system. In Sect. 3, the energy storage optimization model is formulated. The proposed improved rapidly exploring random tree optimizer (IRRTO) algorithm is described in Sect. 4. Section 5 comprises a discussion of the case study results, and Sect. 6 concludes the paper.

2. Vulnerability Indicator System

In practical distribution networks, real-time measurements of nodal voltage magnitudes and power flows are typically obtained through voltage and power sensors at critical nodes and feeder terminals, providing essential data support for vulnerability assessments. To scientifically assess the weak links in distribution networks with high penetration of renewable energy, we constructed a vulnerability indicator system that considers both line and node operational states. The key vulnerability indicators for lines and nodes are defined separately below.

The criticality of a distribution line in facilitating power flow is characterized by its electrical betweenness, defined as

$$b_{mn} = \frac{\sum_{g\in G}\sum_{l\in L}\sqrt{P_g P_l}Y_{gl}\left|I_{gl}(m,n)\right|}{N_g N_l}, (m,n)\in Z \tag{1}$$

$$B_{mn} = \frac{b_{mn}}{\max b_{mn}}, \tag{2}$$

where G denotes the set of generator nodes, P_g is the active power of generator node g, L is the set of load nodes, P_l is the active power of load node l, Y_{gl} is the equivalent admittance between nodes g and l, Z is the set of distribution lines, (m,n) is the line connecting nodes m and n, $I_{gl}(m,n)$ is the current flowing through line (m,n) when a unit current is injected between nodes g and l, and N_g and N_l are the numbers of generator nodes and load nodes, respectively.

By means of power flow calculations, the static voltage stability index of distribution lines is employed to evaluate line vulnerability, and it is expressed as

$$L_{mn,t} = \frac{4(P_{n,t}X_{mn} - Q_{n,t}R_{mn})^2 + 4(P_{n,t}R_{mn} + Q_{n,t}X_{mn})U_{m,t}^2}{U_{m,t}^4}. \tag{3}$$

Here, $P_{n,t}$ and $Q_{n,t}$ are the active and reactive loads at node n at time t, respectively, R_{mn} and X_{mn} are the resistance and reactance of line (m,n), respectively, and $U_{m,t}$ is the voltage magnitude at node n at time t.

The overall vulnerability level of a distribution line is characterized as

$$lf_{mn,t} = \alpha_1 B_{mn} + \alpha_2 L_{mn,t}, \tag{4}$$

$$LF_t^s = \sum_{(m,n)\in Z} lf_{mn,t}, \tag{5}$$

where α_1 and α_2 are weighting coefficients.

To assess the uniformity of line vulnerability distribution across the network, the line vulnerability balance index is defined as

$$LF_t^v = 1 - \left[\frac{-\sum_{(m,n)\in Z} lf_{mn,t} \log_2 \left(lf_{mn,t} \right)}{\log_2 M} \right]^{2\pi}. \tag{6}$$

Here, M is the total number of lines in the distribution network.

The improved node betweenness reflects the criticality of a node in power transmission paths, and it is calculated as

$$B_i^N = \frac{\sum_{g\in G}\sum_{l\in L}\sqrt{P_g P_l} W_{gl}(i) \big/ W_{gl}}{P_b}. \tag{7}$$

Here, W_{gl} denotes the total number of shortest paths between nodes g and l, and $W_{gl}(i)$ is the number of those shortest paths passing through node i.

To directly assess voltage vulnerability, the deviation of a node's voltage magnitude from its nominal level is defined as

$$v_{i,t} = \left| \frac{U_{i,t} - U_{rv}}{\Delta U_{max}} \right|, \tag{8}$$

$$V_{i,t} = \frac{v_{i,t} - v_{i,t}^{min}}{v_{i,t}^{max} - v_{i,t}^{min}}. \tag{9}$$

Here, U_{rv} is the rated voltage, $U_{i,t}$ is the voltage magnitude at node i at time t, ΔU_{max} is the maximum voltage deviation, $v_{i,t}$ is the voltage vulnerability of node i at time t, and $v_{i,t}^{max}$ and $v_{i,t}^{min}$ are the maximum and minimum voltage vulnerability values of node i at time t, respectively.

The node vulnerability is jointly determined by the structural betweenness and voltage vulnerability and is expressed as

$$of_{i,t} = \beta_1 B_i^N + \beta_2 V_{i,t}, \tag{10}$$

$$OF_t^s = \sum_{i \in N} of_{i,t}, \tag{11}$$

where β_1 and β_2 are weighting coefficients.

The node vulnerability balance index, which is a measure of the uniformity of node vulnerability distribution, is defined as

$$OF_t^v = 1 - \left[\frac{-\sum_{i \in N} of_{i,t} \log_2 \left(of_{i,t} \right)}{\log_2 N} \right]^{2\pi}. \tag{12}$$

Here, N is the total number of nodes in the system.

Furthermore, the overall system's vulnerability index is defined as

$$SF = \frac{1}{T} \sum_{t=1}^{T} \sqrt{\lambda_1 LF_t^v \cdot LF_t^s + \lambda_2 OF_t^v \cdot OF_t^s}. \tag{13}$$

Here, T is the total number of operating time periods, and λ_1 and λ_2 are weighting coefficients.

3. System Model

In this study, we aim to coordinate the vulnerability and economic performance of distribution networks by establishing an energy storage optimization configuration framework that incorporates objective functions and system operating constraints.

3.1 Objective functions

The objective function representing the system vulnerability is defined as

$$F_1 = SF. \tag{14}$$

The economic objective function is expressed as

$$F_2 = C_{in} + C_{om} + C_{op}. \tag{15}$$

Here, C_{in} is the average annual investment cost of the ESS, C_{om} is the operation and maintenance cost of the ESS, and C_{op} is the annual operating cost of the distribution network.

The average annual investment cost of the ESS is calculated as

$$C_{in} = \frac{\tau(1+\tau)^y}{365(1+\tau)^y - 1} \sum_{k=1}^{N_b} \left(C_e E_{B,k} + C_p P_{B,k} \right), \tag{16}$$

where τ is the discount rate, y is the service lifetime of the energy storage equipment, N_b is the number of ESSs, C_e is the investment cost per unit energy capacity of each ESS, $E_{B,k}$ is the rated energy capacity of the k-th ESS, C_p is the investment cost per unit power of each ESS, and $P_{B,k}$ is the rated power of the k-th ESS.

The operation and maintenance cost of the ESS is given by

$$C_{om} = C_m \sum_{k=1}^{n} \left(C_e E_{B,k} + C_p P_{B,k} \right). \tag{17}$$

Here, C_m is the operation and maintenance coefficient of the ESS.

The annual operating cost of the distribution network is expressed as

$$C_{op} = \sum_{i=1}^{M} d_i \left(C_{pu} + C_{loss} \right). \tag{18}$$

Here, d_i is the probability of occurrence of scenario i, M is the total number of scenarios, C_{pu} is the electricity purchasing cost, and C_{loss} is the cost of network power loss.

The electricity purchasing cost is calculated as

$$C_{pu} = \sum_{t=1}^{24} e_t P_{pu,t} \Delta t, \tag{19}$$

where e_t is the price of electricity at time t, $P_{pu,t}$ is the power purchased from the upstream grid at time t, and Δt is the duration of each time period.

The cost of network power loss is calculated as

$$\begin{cases} C_{loss} = \sum_{t=1}^{24} e_t P_{loss,t}, \\ P_{loss,t} = \sum_{l=1}^{M} \left[G_{ij} (U_{i,t}^2 + U_{j,t}^2 - 2U_{i,t}U_{j,t} \cos\theta_{ij,t}) \right], \end{cases} \tag{20}$$

with $P_{loss,t}$ being the network power loss at time t, G_{ij} the real part of the mutual admittance between nodes i and j, $U_{i,t}$ the voltage magnitude at node i at time t, and $\theta_{ij,t}$ the voltage phase angle difference between nodes i and j at time t.

To balance system security and economic performance, the overall objective function is formulated as

$$F = c_1 F_1 + c_2 F_2. \tag{21}$$

Here, c_1 is the weighting coefficient of the vulnerability objective, and c_2 is the weighting coefficient of the economic objective.

3.2 Constraints

Power balance constraints at nodes are

$$\begin{cases} P_{i,t} = U_{i,t} \sum_{j=1}^{E_i} U_{j,t} \left(G_{ij} \cos\theta_{ij,t} + B_{ij} \sin\theta_{ij,t} \right), \\ Q_{i,t} = U_{i,t} \sum_{j=1}^{E_i} U_{j,t} \left(G_{ij} \sin\theta_{ij,t} - B_{ij} \cos\theta_{ij,t} \right). \end{cases} \tag{22}$$

Here, $P_{i,t}$ is the injected active power at node i at time t, $Q_{i,t}$ is the injected reactive power at node i at time t, B_{ij} is the imaginary part of the mutual admittance between nodes i and j, $\theta_{ij,t}$ is the voltage phase angle difference between nodes i and j at time t, and E_i is the number of nodes connected to node i.

Node voltage constraints ($U_{i,t}$) are constrained as

$$U_{i,min} \le U_{i,t} \le U_{i,max}. \tag{23}$$

Here, $U_{i,min}$ is the minimum allowable voltage magnitude at node i, and $U_{i,max}$ is the maximum allowable voltage magnitude at node i.

State of charge (SOC) constraints of ESSs are

$$SOC_k(t) = SOC_k(t-1) + \frac{P_{cha,k}(t) \cdot \eta_{cha} \Delta t}{E_{B,k}} + \frac{P_{dis,k}(t) \Delta t}{\eta_{dis} \cdot E_{B,k}}, \tag{24}$$

$$\begin{cases} SOC_{min} \le SOC_k(t) \le SOC_{max}, \\ SOC_k(1) = 50\%, \end{cases} \tag{25}$$

where $SOC_k(t)$ is the state of charge of the k-th energy storage system (ESS) at time t; $P_{cha,k}(t)$ and $P_{dis,k}(t)$ are the charging power and discharging power of the k-th ESS during time t, respectively; η_{cha} and η_{dis} are the charging efficiency and discharging efficiency of the ESS, respectively; SOC_{max} and SOC_{min} are the maximum and minimum allowable limits of the state of charge, respectively.

4. Optimization Method

The proposed IRRTO is developed on the basis of the rapidly exploring random tree optimizer (RRTO).[15] To address the issues of unbalanced exploration and exploitation capabilities at different search stages, three key strategies are introduced: a cubic chaotic map, a step-size learning factor, and a Lévy flight perturbation mechanism.

4.1 Cubic chaotic map

Aimed at augmenting the heterogeneity of the initial solution set and bolstering the algorithm's exploratory prowess, a cubic chaotic map is adopted to initialize the population. The Cubic chaotic mapping is defined as

$$z_{x+1} = \rho \cdot z_x \cdot \left(1 - z_x^2\right), \tag{26}$$

where z_x is the chaotic value at the x-th iteration, and ρ is the control parameter.

The chaotic sequence generated by the cubic map is mapped to the solution space to obtain the initial position of individuals as

$$q_x = b_l + z_x \cdot \left(b_u - b_l\right). \tag{27}$$

Here, q_x is the initial position of the x-th individual, b_u is the upper bound vector of the search space, and b_l is the lower bound vector of the search space.

4.2 Step-size learning factor

Although the global exploration step size of the original RRTO can be adaptively adjusted during iterations, it does not fully exploit historical search experience. To overcome this limitation, a step-size learning factor is designed to enable the algorithm to adaptively regulate the magnitude of the global exploration step size on the basis of historical search performance.

First, the success rate of the global exploration strategy at generation t is defined as

$$\rho_g(s) = (1-\beta)\cdot\rho_g(s-1) + \beta\cdot\phi_g(s), \tag{28}$$

with $\rho_g(s)$ being the success rate of the global exploration strategy at generation s, $\phi_g(s)$ the proportion of individuals whose fitness is improved after applying the global exploration strategy at generation s, and β the forgetting factor used to balance historical and current information.

Using the success rate, the step-size learning factor is calculated as

$$\eta_g(s) = \eta_{min} + (\eta_{max} - \eta_{min})\cdot\frac{\rho_g(s) - \rho_{min}}{\rho_{max} - \rho_{min}}. \tag{29}$$

Here, $\eta_g(s)$ is the step-size learning factor at generation s, η_{min} is the minimum value of the learning factor, η_{max} is the maximum value of the learning factor, ρ_{min} is the predefined lower bound of the success rate, and ρ_{max} is the predefined upper bound of the success rate.

Finally, the improved global exploration step size is updated as

$$s_1^{new} = \eta_g(s)\cdot s_1. \tag{30}$$

Here, s_1^{new} is the updated global exploration step size, and s_1 is the original global exploration step size in the RRTO algorithm.

By incorporating the step-size learning factor, the algorithm expands the exploration step size when the global exploration strategy remains effective, thereby accelerating the exploration of unexplored regions. Conversely, when the success rate declines, the step size is reduced to perform more cautious exploration.

4.3 Lévy flight perturbation

To circumvent entrapment in local optima, particularly during the later search phases, a Lévy flight perturbation mechanism is incorporated into the local search strategy. After an individual completes the original local search strategy, a Lévy flight perturbation is applied with a probability of p_t. The final position of the individual after perturbation is determined as

$$q_x^{final}(s) = q_x^{new}(s) + p_L(s)\cdot L(\lambda)\cdot(b_u - b_l), \tag{31}$$

where $q_x^{final}(s)$ is the final position of the x-th individual at iteration s after Lévy flight perturbation, $q_x^{new}(s)$ is the position obtained after the original local search strategy, $L(\lambda)$ is the Lévy-distributed random step-size vector generated by the Mantegna algorithm with characteristic exponent λ, and $p_L(s)$ is the Lévy flight perturbation-triggering probability at iteration s.

The perturbation-triggering probability is introduced to vary with the iteration number, as expressed by

$$p_L(s) = p_{L_{min}} + \left(p_{L_{max}} - p_{L_{min}}\right) \cdot (s / S). \tag{32}$$

Here, $p_{L_{min}}$ is the minimum triggering probability, $p_{L_{max}}$ is the maximum triggering probability, s is the current iteration number, and S is the maximum number of iterations.

Through this algorithm, as the iteration proceeds and the algorithm gradually converges, the probability of introducing Lévy flight perturbations increases.

4.4 Algorithm flow

Figure 1 illustrates the overall flowchart of the proposed IRRTO algorithm. The flow integrates cubic chaotic initialization, global exploration enhanced by the step-size learning factor, and local search combined with Lévy flight perturbation. The complete optimization process, from parameter initialization to the output of the optimal solution, is clearly depicted.

5. Case Study

5.1 Parameter settings

In this study, photovoltaic generation, wind power generation, and load data from a region in Hebei Province, China, are adopted for simulation analysis using the standard IEEE 33-node

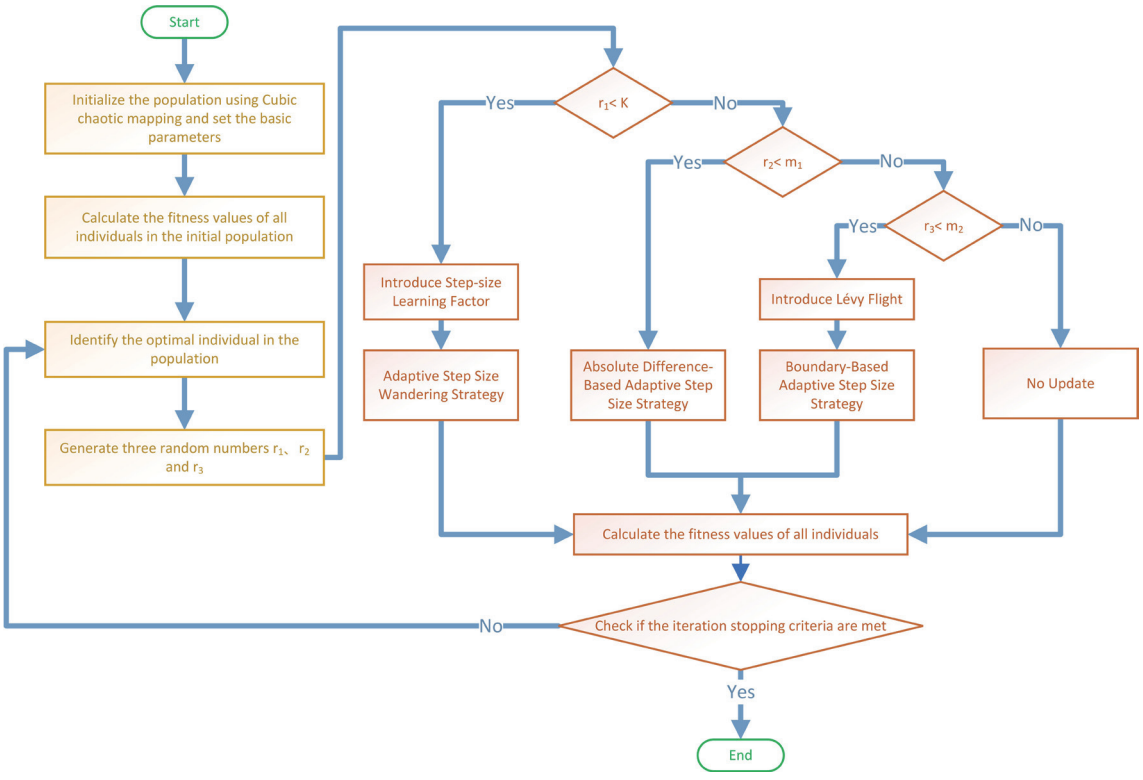

Fig. 1. (Color online) Flowchart of the proposed IRRTO algorithm.

distribution network. As depicted in Fig. 2, the system configuration comprises photovoltaic units at nodes 21 (1400 kW) and 30 (2100 kW), a wind generator at node 14 (1500 kW), and a thermal power plant at node 9 (500 kW). The candidate nodes for energy storage installation are set as {3, 10, 16, 20, 24, 31}. The key ESS parameters are detailed in Table 1.

To reduce computational complexity while preserving the representative characteristics of renewable generation and load profiles, the original data set is clustered using the density-based spatial clustering of applications with noise (DBSCAN) algorithm. Accordingly, four typical scenarios are obtained, with the corresponding occurrence probabilities of 21.18, 28.06, 21.70, and 24.06%, respectively, as illustrated in Fig. 3, covering the photovoltaic generation scenario, wind power generation scenario, and load demand scenario.

5.2 Discussion of configuration results

For the assessment of the developed model and algorithm performances, the following cases are compared.

Case 1: No ESS is installed

Case 2: Energy storage optimization configuration based on the conventional RRTO algorithm

Case 3: Energy storage optimization configuration based on the proposed IRRTO algorithm

Table 2 shows the energy storage planning outcomes for Case 2 and Case 3, while Table 3 provides a summary of the corresponding simulation results across all schemes.

As shown in Tables 2 and 3, the IRRTO-based scheme (Case 3) achieves the best overall performance among all configurations in terms of system security and economic efficiency.

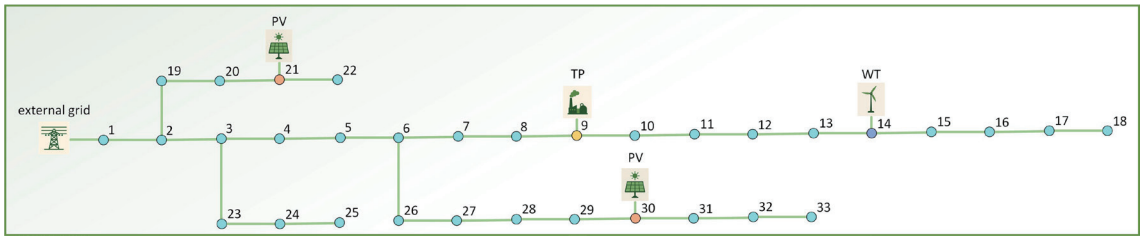

Fig. 2. (Color online) Standard IEEE 33-node distribution network.

Table 1
Basic parameters of ESS.

Parameter	Value
C_e	2100 yuan/kWh
C_p	1000 yuan/kW
C_m	5%
η_{cha}	90%
η_{dis}	90%
τ	0.06
y	15 years
$[SOC_{min}, SOC_{max}]$	[0.1,0.9]

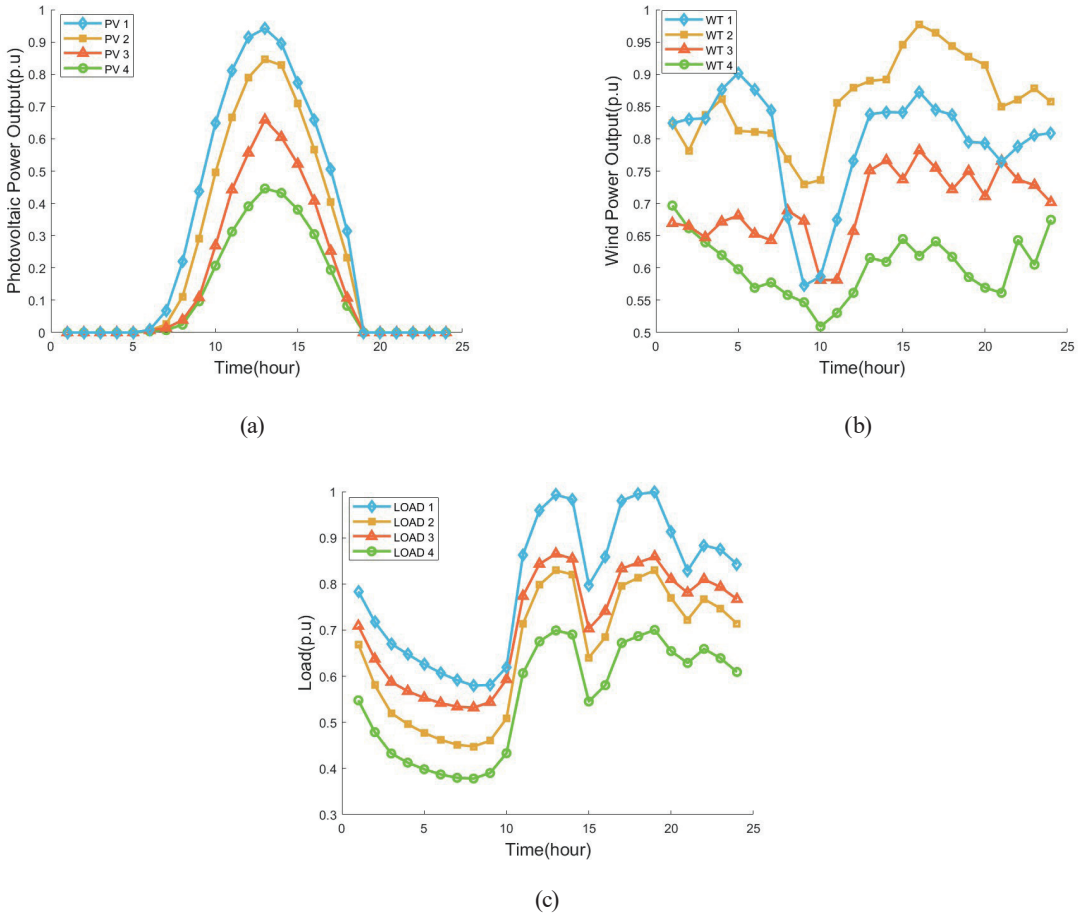

Fig. 3. (Color online) Performance outcomes under different scenarios. (a) Photovoltaic generation scenario. (b) Wind power generation scenario. (c) Load demand scenario.

Table 2
ESS configuration schemes for Case 2 and Case 3.

	DESS node number	DESS energy capacity (kWh)	DESS power capacity (kW)
Case 2	(3,16)	(1200,1730)	(360,520)
Case 3	(10,31)	(1090,1600)	(330,480)

Table 3
Cost and voltage deviation for the different schemes.

	F_1	V (p.u)	C_{in} (yuan)	C_{pu} (yuan)	C_{loss} (yuan)
Case 1	0.687	0.3743	0	28457	3532.11
Case 2	0.573	0.3275	2066.31	24626	2558.71
Case 3	0.529	0.2732	1897.05	24492	2058.54

Compared with Case 1 and Case 2, the vulnerability index is reduced by 23.0 and 7.7%, while voltage deviation decreases by 27.0 and 16.6%, respectively, indicating improved voltage quality and operational stability. Economically, Case 3 requires a lower energy storage investment cost than Case 2 (8.2% reduction). In addition, electricity purchasing and network loss costs are

reduced by 13.9 and 41.7% compared with Case 1, and by 0.55 and 19.6% compared with Case 2, respectively. These results indicate that the proposed IRRTO algorithm enables more economical energy storage planning while significantly enhancing system security and operational performance.

The variations in the vulnerability index and active power losses of the different schemes are illustrated in Fig. 4. It shows the temporal variations of the vulnerability index (*SF*) and network power losses for the three schemes. The results indicate a high correlation between system vulnerability, renewable generation, and load demand. In Case 1, between 00:00 and 09:00, both load demand and renewable output remain low, and the system operates far from the stability boundary, resulting in the lowest vulnerability level. From 10:00 to 15:00, the increasing photovoltaic and wind power outputs, combined with rising load demand, lead to voltage deviations and uneven power flow distribution, causing vulnerability to increase and reach a peak at around midday. At approximately 15:00, the vulnerability temporarily decreases owing to reduced load demand. Between 16:00 and 24:00, as photovoltaic output diminishes and wind generation stays elevated, the line voltage magnitudes drop so that the system vulnerability increases.

After integrating energy storage, the *SF* and power loss curves in Case 2 and Case 3 unveil an overall downward shift and smoother variation, indicating effective peak shaving and valley filling. Notably, during periods of high renewable fluctuations around midday and load peaks at night, Case 3 consistently achieves the lowest *SF* values and network power losses.

The voltage profile of Case 3 under a typical scenario is shown in Fig. 5(a), and the node voltage variation at the 19th hour under different schemes is shown in Fig. 5(b). From the voltage surface plots and the voltage distribution at the 19th hour, Case 1 exhibits marked voltage fluctuations owing to the lack of any ESS, where the voltages at multiple nodes approach the lower operational bound during peak load hours. In Case 2, the energy storage installed at nodes 3 and 16 primarily has lower voltage deviation for nodes 3–18, while nodes 19–33 still operate near the lower limit. By contrast, in Case 3, with energy storage deployed at nodes 10 and 31,

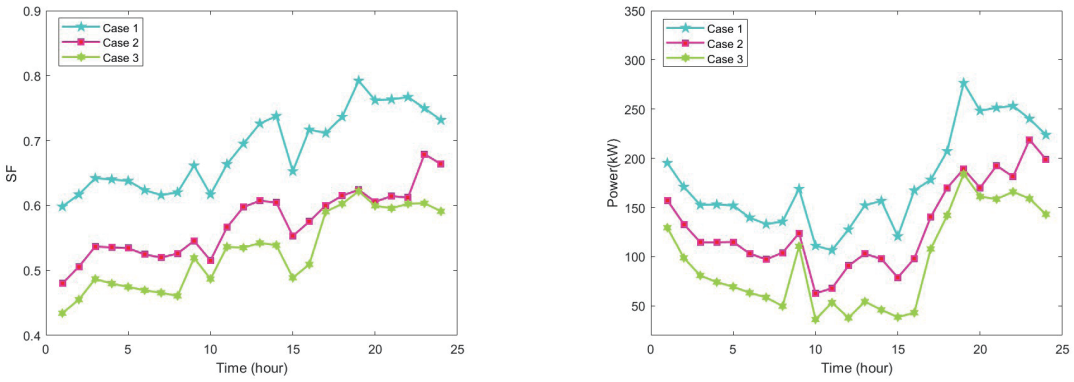

(a) (b)

Fig. 4. (Color online) Vulnerability and active power loss of the three schemes. (a) *SF* values. (b) Network power loss.

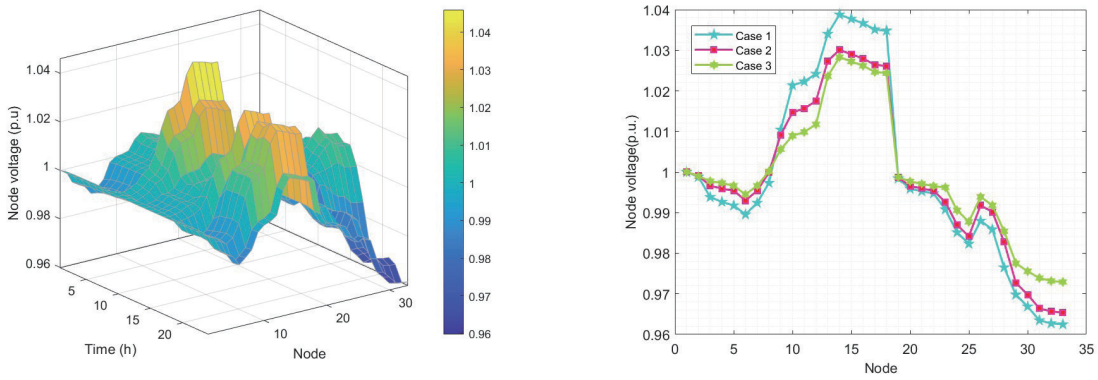

(a) (b)

Fig. 5. (Color online) Voltage variations under the different schemes. (a) Voltage profile of Case 3 under typical scenario. (b) Voltage variation over nodes at the 19th hour under different schemes.

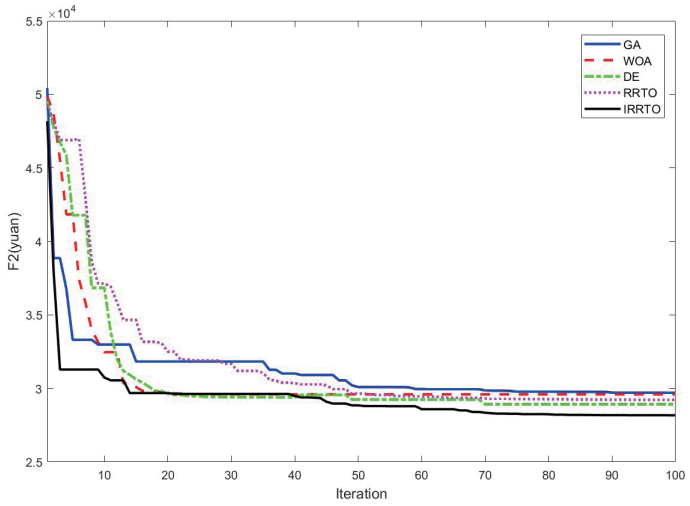

Fig. 6. (Color online) Convergence curves using different optimization algorithms.

there is a more uniform voltage distribution and effective mitigation of voltage deviation across nodes 19–33, attaining the smallest overall voltage deviation.

To assess the performance of the proposed IRRTO algorithm, four benchmark methods, namely, genetic algorithm (GA), differential evolution (DE), whale optimization algorithm (WOA), and the original RRTO algorithm, are employed for comparison. The convergence process of the economic objective value, shown in Fig. 6, is used as the evaluation criterion.

As can be seen, GA, WOA, DE, and RRTO exhibit premature convergence, being trapped into local optima. On the other hand, the proposed IRRTO improves the initial population diversity and achieves wide exploration in early iterations with fast convergence.

6. Conclusions

In response to the need for the assurance of security and economic performance in renewable-rich distribution networks, we carried out vulnerability-aware energy storage planning and configuration. The key findings of this study are summarized below.

(1) By incorporating line- and node-level vulnerability indices with a cost model, the proposed framework provides effective decision support for secure and economical energy storage deployment.
(2) By introducing a step-size learning factor and a Lévy flight perturbation mechanism, the algorithm attains an equilibrium of the exploration–exploitation trade-off, leading to an accelerated convergence rate and enhanced solution precision.
(3) Compared with the case without energy storage, the IRRTO-based configuration reduces the system vulnerability and voltage deviation by up to 23.0 and 27.0%, respectively.
(4) Compared with the conventional RRTO-based scheme, the system vulnerability and voltage deviation are further reduced by 7.7 and 16.6%, respectively, while requiring lower energy storage investment and operating costs.

In future work, we plan to focus on coordinated optimization with other flexible resources and the impacts of increased uncertainties and market complexity.

Acknowledgments

This study was supported by Project No. 202305B029 and Tianjin Carbon Peak and Carbon Neutrality Technology Major Project (Grant no. 24ZXTKSN00030) and Tianjin Natural Science Foundation Project (Grant no. 23JCQNJC01060).

References

1 M. Alrashidi and S. Rahman: Int. J. Electr. Power Energy Syst. **151** (2023) 109217. https://doi.org/10.1016/j.ijepes.2023.109217
2 L. M. Zhang, H. X. Ye, Y. Y. Ge, and Z. Y. Li: IEEE Trans. Power Syst. **40** (2025) 2519. https://doi.org/10.1109/tpwrs.2024.3467276
3 S. Mohanty, M. R. Nayak, and A. Gantayet: Computers & Electrical Engineering **119** (2024) 109616. https://doi.org/10.1016/j.compeleceng.2024.109616
4 X. R. Sun, L. Y. Lin, S. Wu, X. M. Zhai, C. H. Jin, and X. P. Pan: J. Energy Storage **133** (2025) 117949. https://doi.org/10.1016/j.est.2025.117949
5 M. J. Du, P. Guo, E. Zio, and J. Zhao: Reliab. Eng. Syst. Saf. **260** (2025) 111058. https://doi.org/10.1016/j.ress.2025.111058
6 X. Li, Y. H. Shi, R. Zhang, X. D. Zhang, R. L. Tang, X. G. Yang, J. G. Lai, and Y. Zhang: Sustainable Energy Grids Networks **43** (2025) 101724. https://doi.org/10.1016/j.segan.2025.101724
7 S. H. Huang, S. W. Guo, L. Y. Xiong, Y. Zhou, F. Gao, W. T. Huang, Q. A. Jia, and Y. Li: J. Energy Storage **141** (2026) 119075. https://doi.org/10.1016/j.est.2025.119075
8 X. W. Wang, Q. K. Kang, J. Gao, F. Zhang, X. Wang, X. Y. Qu, and L. Guo: Energy **289** (2024) 129825. https://doi.org/10.1016/j.energy.2023.129825
9 Z. Ullah, H. S. Qazi, A. Alferidi, M. Alsolami, B. Lami, and H. M. Hasanien: J. Energy Storage **108** (2025) 115005. https://doi.org/10.1016/j.est.2024.115005
10 J. J. A. Saldanha, A. Nied, R. Trentini, and R. Kutzner: Electr. Power Syst. Res. **234** (2024) 110554. https://doi.org/10.1016/j.epsr.2024.110554
11 W. Wang, X. Q. Zhang, L. Fu, M. K. Liao, and X. M. Xu: J. Energy Storage **80** (2024) 110157. https://doi.org/10.1016/j.est.2023.110157

12 B. X. Ji, H. H. Liu, P. Cheng, X. Y. Ren, H. D. Pi, and L. L. Li: J. Energy Storage **91** (2024) 112093. https://doi.org/10.1016/j.est.2024.112093
13 A. Ali, A. U. R. Bughio, G. Abbas, M. U. Keerio, N. H. Mugheri, S. Memon, and A. S. Saand: Energy **311** (2024) 133463. https://doi.org/10.1016/j.energy.2024.133463
14 N. Belbachír, S. Kamel, M. H. Hassan, and M. Zellagui: J. Energy Storage **78** (2024) 110288. https://doi.org/10.1016/j.est.2023.110288
15 G. J. Lai, T. Li, and B. J. Shi: IEEE Access **13** (2025) 42744. https://doi.org/10.1109/access.2025.3547537